PAPER

Influence of particle size, cycling rate and temperature on the lithiation process of anatase TiO$_2$†

H. Liu and C. P. Grey*

The nature of a phase transition plays an important role in controlling the kinetics of reaction of an electrode material in a lithium-ion battery. The actual phase transition path can be affected by particle size and cycling rate. In this study, we investigated the phase transition process during the electrochemical Li intercalation of anatase TiO$_2$ as a function of particle size (25 nm and 100 nm), cycling rate (1C, 2C, 5C, 10C, 20C) and temperature (room temperature and 80 °C) by *in situ* synchrotron X-ray diffraction. The phase transition was found to be affected by the particle size: the 100 nm particles react simultaneously *via* a conventional nucleation and growth, *i.e.* two-phase, mechanism, while the 25 nm particles react sequentially *via* a two-phase mechanism. The Li miscibility gap decreases with increasing cycling rate, yet the phase separation was not suppressed even at a cycle rate of 20C. An increase in temperature from room temperature to 80 °C significantly improves the electrode's electrochemical performance despite undergoing a two-phase reaction. The failure to observe a continuous structural transition from tetragonal TiO$_2$ to orthorhombic Li$_{0.5}$TiO$_2$ even at high rates and elevated temperature was attributed to the high energy barrier of a continuous phase transition path.

Introduction

Most commercial Li ion battery electrodes employ intercalation compounds, such as LiCoO$_2$ and LiFePO$_4$, where Li insertion and extraction can be reversibly extracted from and inserted into the host structure during battery charge and discharge, respectively. For intercalation compounds, (de)lithiation takes place either by a single-phase reaction, where the host structure forms a solid solution with Li within a certain Li composition range, or by a two-phase reaction, where a first-order phase transition is induced as Li is (de)intercalated. A single-phase reaction, which proceeds *via* a continuous structural change and avoids nucleation of a second phase, is generally considered to be important for fast reaction kinetics and is thought to be more favourable than a two-phase reaction for long-term capacity retention of the battery. Recent studies have identified a non-equilibrium single-phase transition mechanism in nanoparticulate LiFePO$_4$ (ref. 1 and 2) and LiNi$_{1/2}$Mn$_{3/2}$O$_4$,[3] electrode materials that are generally thought to transform *via* a two-phase mechanism at low cycling rates. The possibility that a two-phase material can transform *via* a single-phase mechanism under non-equilibrium conditions opens up new avenues for the search of new electrode compounds and begs the

question as to how prevalent this phenomenon is in compounds that exhibit a thermodynamic Li miscibility gap (between two compounds with different Li stoichiometries). To complement previous studies, which have only explored compounds that do not involve a change in crystal symmetry between the two end member phases, this work investigates the phase transition of anatase TiO$_2$, which transforms from tetragonal to orthorhombic symmetry upon Li intercalation.

Anatase, TiO$_2$, is used as an anode material for lithium ion batteries and, in theory, can accommodate a maximum of 1 Li per formula unit (f.u.). Initial Li intercalation into anatase TiO$_2$ from $z = 0$ to 0.025 (z in Li$_z$TiO$_2$) proceeds by a single-phase, solid solution reaction.[4] When Li is further intercalated, there is a two-phase reaction in the composition range $0.025 < z < 0.5$ (z in Li$_z$TiO$_2$) between tetragonal Li$_{a \approx 0.025}$TiO$_2$ ($I4_1/amd$, no. 141, Fig. 1A),[5] denoted as the α-TiO$_2$ phase, and orthorhombic Li$_{b \approx 0.5}$TiO$_2$ (*Imma*, no. 74, Fig. 1B),[6] denoted as the β-Li$_{0.5}$TiO$_2$ phase. Further intercalation for $z > 0.5$ is kinetically restricted by very slow Li ion diffusion,[7,8] and as a result, transformation to LiTiO$_2$ ($I4_1/amd$, Fig. 1C), denoted as γ-LiTiO$_2$, is only observed for very small nanoparticles (∼7 nm) and on the surface layer of larger particles at room temperature.[4] The thermodynamics of the system are also dependent on the particle size: for particles larger than 50 nm, both the α-TiO$_2$ and β-Li$_{0.5}$TiO$_2$ phases can coexist in a single particle; for particles smaller than 50 nm, such phase coexistence is not stable, and for overall Li stoichiometries of $0.025 < z < 0.5$ for the whole powder or electrode each individual crystallite is composed entirely of either the α-

Department of Chemistry, University of Cambridge, Lensfield Road, CB2 1EW, UK. E-mail: cpg27@cam.ac.uk

This journal is © The Royal Society of Chemistry 2016

J. Mater. Chem. A, 2016, **4**, 6433–6446 | 6433
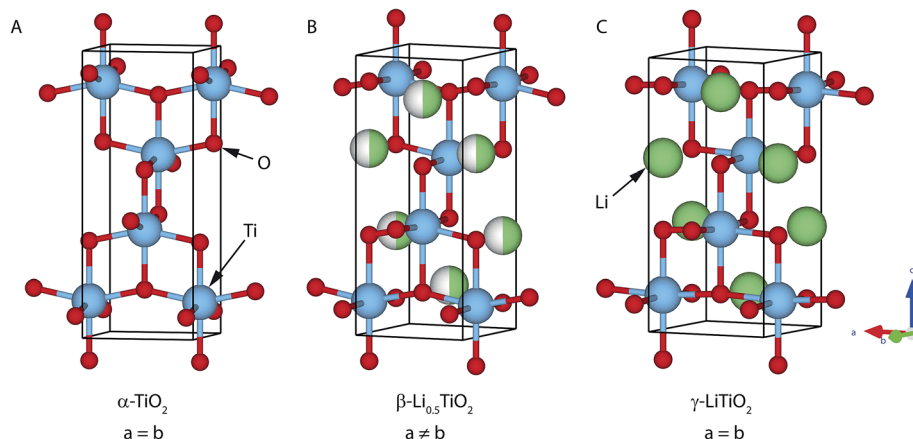
Fig. 1 The crystal structures of (A) tetragonal α-TiO$_2$, (B) orthorhombic β-Li$_{0.5}$TiO$_2$ and (C) tetragonal γ-LiTiO$_2$. The half-filled green/white spheres correspond to sites that are randomly occupied by either a Li or a vacancy with equal probability.

TiO$_2$ or the β-Li$_{0.5}$TiO$_2$ phase.[4] The effect of particle size on the reaction mechanism at a very low rate (C/120) was recently investigated by *in situ* XRD.[9] It was found that both small (15 nm) and large (130 nm) particles react *via* the sequential reaction of particles, *i.e.*, the so-called domino-cascade mechanism proposed originally for nanoparticles of LiFePO$_4$.[10] The same study, despite being carried out at a low rate, also reveals a non-equilibrium nature for the transition between α-TiO$_2$ and β-Li$_{0.5}$TiO$_2$: the Li content of α-TiO$_2$ and β-Li$_{0.5}$TiO$_2$ measured during the transition process of TiO$_2$ → Li$_{0.5}$TiO$_2$ being different than the Li content measured under equilibrium at the same state of overall lithiation, the effect being more pronounced for the 15 nm particles. Hence, it would be interesting to explore whether the deviation from the equilibrium Li composition could be large enough at high rates to achieve a continuous (2nd-order) phase transition between α-TiO$_2$ and β-Li$_{0.5}$TiO$_2$. To this end, the phase transition of anatase TiO$_2$ during electrochemical cycling under different cycling rates and temperatures is investigated here by using *in situ* synchrotron XRD. By following the changes in the Bragg peaks of both α-TiO$_2$ and β-Li$_{0.5}$TiO$_2$ phases during one discharge–charge cycle, we find the nature of the phase transition remains first order regardless of the cycling conditions tested here. Our study suggests the first-order phase transition is more energetically favourable than an overpotential-driven second-order phase transition.

Experimental

Materials and electrode preparation

The 25 nm and 100 nm TiO$_2$ powders were purchased from Sigma Aldrich. The electrode was prepared with a high proportion of carbon additives, to improve the electrochemical performance of the active material at high rates (by increasing the electronic conductivity). For a typical electrode, 3 mg of the active material powder was mixed with Super P carbon (Alfa Aesar), carbon black (Vulcan XC-72, Cabot Corporation) and polytetrafluoroethylene (PTFE) binder (Sigma-Aldrich) in the

mass ratio 3 : 3 : 3 : 1 and was pressed (1.6–1.8 ton) into a pellet of 13 mm in diameter.

Laboratory XRD measurement

The as-purchased anatase TiO$_2$ samples were measured at room temperature on a Panalytical Empyrean diffractometer using Cu Kα radiation. Whole powder pattern fitting was performed with TOPAS software. The peak profile was modelled by the isotropic size broadening. The Voigt peak shape (convolution of Lorentzian and Gaussian peak shape) is used to describe the isotropic size broadening, and 2θ dependence of the peak width is given by

$$H_{iso} = 0.9\lambda/(L\cos(\theta)) \tag{1}$$

where H_{iso} is the full width at half maximum (FWHM) of the Voigt profile, λ is the wavelength of the incident beam, and L is the refined parameter corresponding to the average particle size.

In situ XRD measurement

The electrode pellet was assembled into the AMPIX cell[11] with Li foil as the anode, glass fibre as the separator and 1 M LiPF$_6$ in 1 : 1 ethylene carbonate/dimethyl carbonate (Tomiyama Pure Chemical Industries) as the liquid electrolyte. For high temperature electrochemical cycling, the cell was heated up with a heating tape whose temperature was set to 80 °C by a thermostat. *In situ* synchrotron XRD measurements were performed in transmission geometry at beamline 17-BM of the Advanced Photon Source at Argonne National Laboratory (wavelength 0.72779 Å, 500 μm diameter beam). An area detector (Perkin-Elmer) consisting of 2048 × 2048 pixels of 200 μm × 200 μm in size was used and was placed 400 mm away from the AMPIX cell. The same electrode was used for the *in situ* measurement at different cycling rates, with measurements taken in the order from low to high rate. The data collection time of each sequential pattern for 1C, 2C, 5C, 10C and 20C cycling rates was 30 s, 12 s, 6 s, 3 s, and 3 s, respectively, which corresponds to a change of

6434 | *J. Mater. Chem. A*, 2016, **4**, 6433–6446

This journal is © The Royal Society of Chemistry 2016

View Article Online

Paper | Journal of Materials Chemistry A

Open Access Article. Published on 12 April 2016. Downloaded on 1/17/2026 6:02:36 PM. This article is licensed under a Creative Commons Attribution 3.0 Unported Licence.

0.004 Li, 0.003 Li, 0.004 Li, 0.004 Li and 0.008 Li, respectively, per formula unit (f.u.) of TiO_2 during the collection of each pattern. The C-rate is calculated based on the theoretical capacity of 0.5 Li insertion per f.u., which is 168 mA h g^{-1}. LaB_6 powder was measured to obtain the instrumental broadening profile.

Rietveld refinements were performed with TOPAS software package[12] in the 2θ range 10.3–35.5°. The background was modelled by 4 asymmetrical pseudo-Voigt peaks at positions $\sim$11.7°, $\sim$20.1°, $\sim$25.0°, $\sim$34.8°, respectively, full width at half maximum (FWHM), intensity, shape parameter being refined, to account for the diffraction background intensity from glassy carbon, glass fibre separator and the liquid electrolyte, on top of the function $B/2\theta$, where B was refined. Two phases corresponding to α-TiO_2 ($I4_1/amd$) and β-$Li_{0.5}TiO_2$ ($Imma$) were included in the refinement. The scale factors, unit cell parameters, atomic coordinates and isotropic atomic displacement parameters (ADP) for Ti and O atoms were refined. Ti and O atoms in both phases were constrained to have the same ADP for each atomic species. The peak profile was modelled by the convolution of isotropic size broadening as described in eqn (1) with anisotropic strain-like broadening (both Lorentzian and Gaussain).

The 2θ dependence of the anisotropic strain-like broadening is described by

$$H_{aniso} = \Sigma_{ij}C_{ij}Y_{ij}\tan(\theta) \qquad (2)$$

where H_{aniso} is the FWHM of the Voigt peak profile, Y_{ij} is the symmetrised spherical harmonics,[13] and C_{ij} are the refined parameters. Since the peak broadening was modelled empirically to obtain a good refinement, no microstructural information about the sample was obtained.

Results and discussion

Particle size and electrochemistry of anatase TiO_2

The scanning electron microscope (SEM) images of the as-purchased TiO_2 powder, specified as 100 nm and 25 nm, respectively, are shown in Fig. 2A and B. To confirm the particle size of the two samples, Pawley fitting against the XRD patterns of the as-purchase samples was performed to extract the particle size, and the results are shown in Fig. 2C and D for the 100 nm and the 25 nm samples, respectively. The refined average particle sizes (91 $\pm$ 13 nm and 24.8 $\pm$ 0.5 nm) are in good agreement (within errors) with the specification given by the supplier. (Analysis on the particle size distribution can be found in Fig. S1.†) Henceforward, the two TiO_2 samples are referred to by the size specified by the supplier, *i.e.* 100 nm and 25 nm, respectively.

In situ XRD measurements were conducted for both TiO_2 samples at cycle rates of 1C, 2C and 5C at room temperature and at cycle rates of 5C, 10C and 20C at 80 °C. The same electrode comprised of 25 nm particles was used for both room temperature and 80 °C cycles, while two electrodes made with 100 nm particles were used for room temperature and 80 °C cycling. Cycles were carried out in the order of increasing rates at each

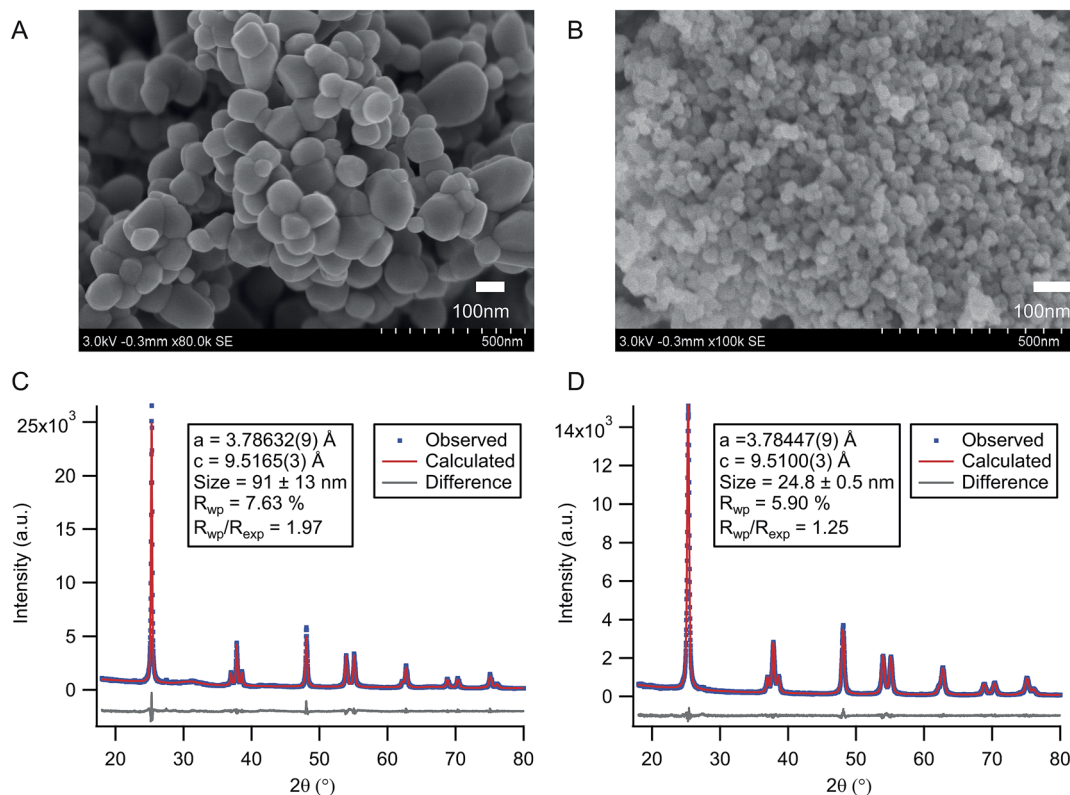Fig. 2 SEM images obtained for (A) 100 nm and (B) 25 nm anatase TiO_2 samples. Pawley fitting results against the XRD patterns of the (C) 100 nm and (D) 25 nm anatase TiO_2 samples.

This journal is © The Royal Society of Chemistry 2016 | *J. Mater. Chem. A*, 2016, **4**, 6433–6446 | **6435**

temperature, for example, 1C, 2C and 5C cycles were carried out sequentially at room temperature. For 25 nm particles, cycling at 80 °C was performed after all the cycling at room temperature had been completed. Discharge and charge were limited to the voltage window 1.0–3.5 V, except for the room temperature 1C and 2C cycling of the 25 nm particles, where the low cut-off voltage was accidently set to 1.2 V. The voltage profiles obtained during the *in situ* XRD experiment are shown in Fig. 3. The *x*-axis corresponds to the total Li inserted or removed per f.u. of TiO_2 and is calculated from the measured experimental capacity assuming 100% coulombic efficiency and is denoted by x; the Li composition of each phase is denoted by z.

For 100 nm particles at 1C cycling at room temperature (Fig. 3A), the discharge voltage profile is consistent with previous report:[14] a steep drop in voltage is followed by a voltage plateau at 1.7 V between $x = 0.05$ and 0.25, corresponding to the transition from α-TiO_2 to β-$Li_{0.5}TiO_2$. The sloping voltage profile towards the end of discharge (from $x = 0.3$ to 0.45 Li) is tentatively attributed to an increased voltage polarisation due to the slow reaction kinetics associated with the transformation of the last fraction of α-TiO_2 to β-$Li_{0.5}TiO_2$, and electrolyte decomposition at low voltages[15,16] to form a protective layer of solid electrolyte interface (SEI). Further Li insertion exceeding $Li_{0.5}TiO_2$ has also been seen by some authors.[17,18] Except for the irreversible SEI formation, the aforementioned process is reversed on charge. The small voltage bump seen on charge at $x = 0.57$ is associated with a kinetic barrier, such as nucleation of a second phase or the slow Li diffusion in γ-$LiTiO_2$, which may form as a surface layer. The voltage profiles under other cycling conditions exhibit similar behaviour.

Phase evolution of anatase TiO_2 under various conditions

Image plots of the time-resolved *in situ* XRD patterns for the evolution of the (024) reflection of α-TiO_2 and the (204)

reflection of β-$Li_{0.5}TiO_2$ during high rate cycling at room temperature are shown in Fig. 4A–C for 100 nm particles and Fig. 4D–F for 25 nm particles. (024) and (204) are symmetry equivalent reflections in tetragonal α-TiO_2, but not in orthorhombic β-$Li_{0.5}TiO_2$. If the transition from the tetragonal to the orthorhombic phase is continuous, one would expect to observe, in the *in situ* XRD patterns, the branching of the (024) reflection into two reflections, (204) and (024), and then the continuous shift of these reflections towards the 2θ values of the β-$Li_{0.5}TiO_2$ (204) and (024) reflections, respectively. For clarity, the (024) reflection of β-$Li_{0.5}TiO_2$, which appears at a lower 2θ angle but overlaps with other peaks, is not shown. On discharging the 100 nm particles at a cycle rate of 1C (Fig. 4A), the (024) reflection of α-TiO_2 shifts to a lower 2θ angle (0–0.07 overall cycled Li per f.u.) at the beginning of discharge, indicating an increase in the Li content of α-TiO_2 *via* a single-phase reaction; further discharge shows a characteristic two-phase reaction, where the (204) reflection of β-$Li_{0.5}TiO_2$ grows at the expense of the (024) reflection of α-TiO_2. On discharge, the (204) reflection of β-$Li_{0.5}TiO_2$ decreases in intensity and the (024) reflection of α-TiO_2 is restored. A similar evolution of the (024) reflection of α-TiO_2 is observed for the 100 nm particles at cycle rates of 2C and 5C, as shown in Fig. 4B and C, respectively; however, due to the limited extent of formation of β-$Li_{0.5}TiO_2$ on discharging at higher rates, the intensity of the (204) reflection of β-$Li_{0.5}TiO_2$ becomes very weak at 2C, as reflected by the single contour level corresponding to ~9% maximum intensity of the image (Fig. 4B) seen for this reflection; it is barely visible at 5C, where the intensity of the β-$Li_{0.5}TiO_2$ (204) reflection is less than ~9% (Fig. 4C). The diffraction patterns shown in Fig. 4D–F are qualitatively similar to those of the 100 nm particles and also display features of the two-phase reactions. The 25 nm particles show improved kinetics as indicated by the higher fraction of
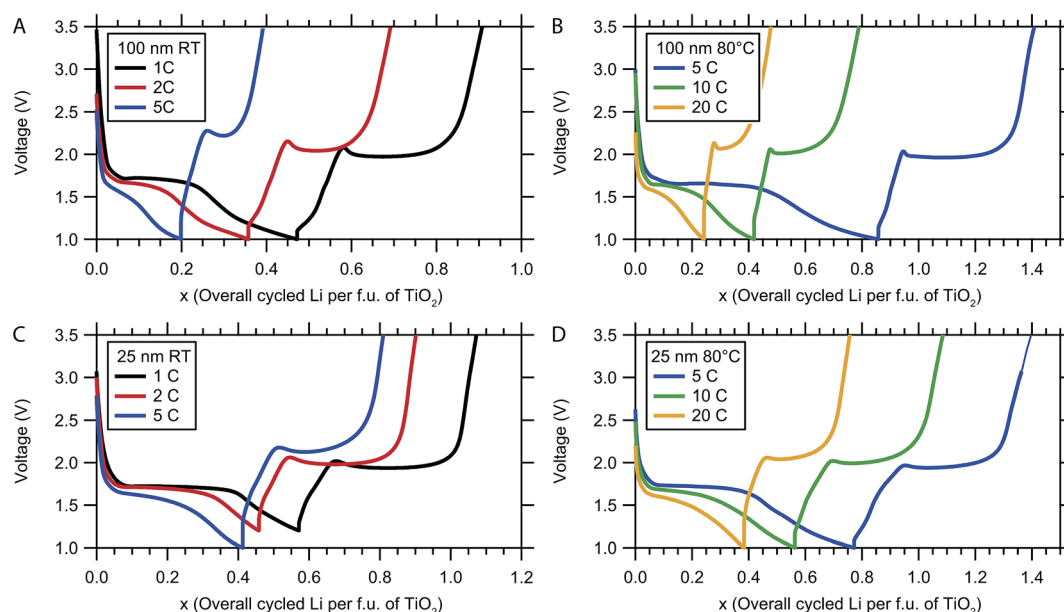
Fig. 3 Voltage profiles for the discharge–charge cycles performed during the *in situ* XRD experiment. (A) Room temperature (RT) and (B) 80 °C cycling for 100 nm particles. (C) Room temperature and (D) 80 °C cycling for 25 nm particles.
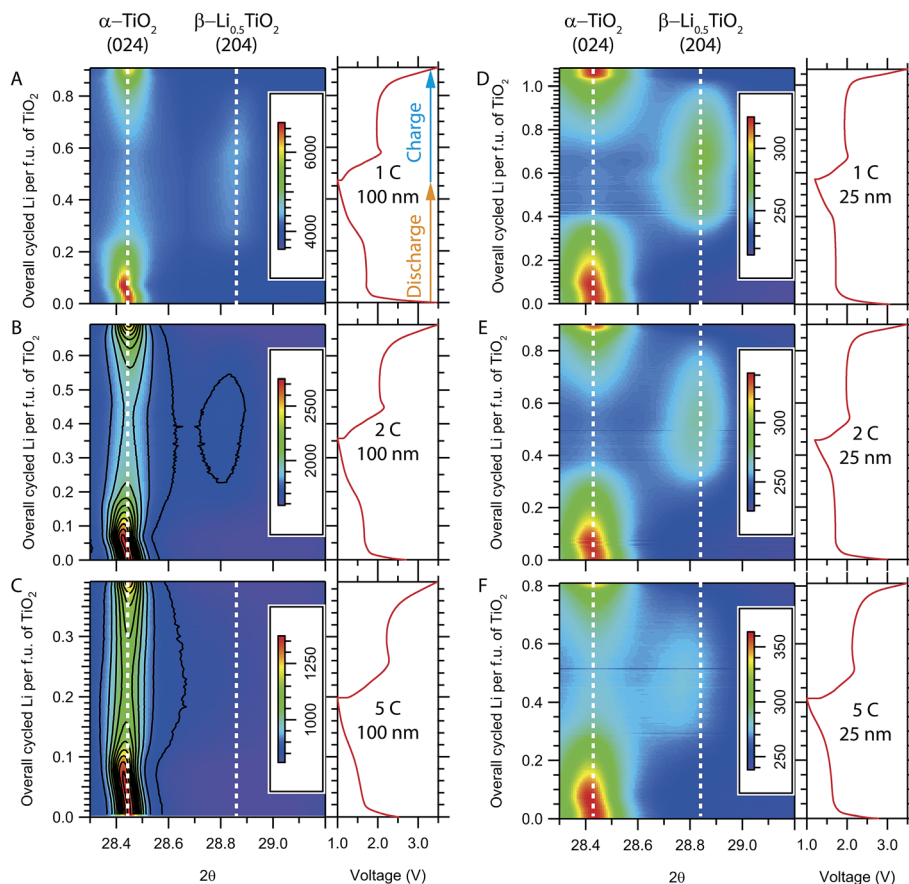
Fig. 4 Image plots showing the time evolution of the *in situ* XRD patterns at room temperature for (A–C) 100 nm and (D–F) 25 nm TiO$_2$ particles at various cycling rates. The intensity scale is shown by the colour bar. The electrochemical profile is shown in the graph to the right of each image. Only the 2θ region for the (024) reflection of α-TiO$_2$ and the (204) reflection of β-Li$_{0.5}$TiO$_2$ is shown. The (204) reflection of β-Li$_{0.5}$TiO$_2$ is barely visible in B and C due to the formation of a very limited amount of β-Li$_{0.5}$TiO$_2$; the equally-spaced intensity contours (11 levels in total) are drawn in black in these figures to aid visual inspection.

the β-Li$_{0.5}$TiO$_2$ formed and the higher discharge capacity at the end of discharge in comparison to the 100 nm particles at equivalent rate: for example, the discharge capacity of 25 nm particles at 5C corresponds to the insertion of 0.4 Li per f.u. as opposed to 0.2 Li for 100 nm particles at the same rate.

Since the (dis)charge process at room temperature terminates prematurely at higher rates (≥5C), to probe the phase transition at rates above 5C, electrochemical cycling was performed at an elevated temperature (~80 °C) to improve the Li diffusion and the reaction kinetics; the corresponding *in situ* XRD patterns are shown in Fig. 5. While there is a noticeable improvement in the rate performance of both 100 nm and 25 nm particles with the formation of a substantial amount of β-Li$_{0.5}$TiO$_2$ at the end of the 20C discharge, the XRD patterns still exhibit characteristic two-phase behaviour for both particles sizes. Visual inspection of the *in situ* XRD patterns suggest the delithiation undergoes the same mechanism as lithiation, therefore, only the analysis and discussion of the lithiation process are presented in this article.

Evolution of lattice parameters and phase fractions

Rietveld refinements were carried out to follow the evolution of the α-TiO$_2$ and β-Li$_{0.5}$TiO$_2$ lattice parameters and capture any

quantitative differences in the phase transition between the various cycling conditions. Typical fitting patterns and R_{wp} factors can be found in Fig. S2 and S3,† respectively. The refined lattice parameters as a function of the overall Li composition determined from the electrochemistry during discharge are shown in Fig. 6. The evolution of the α-TiO$_2$ lattice parameters exhibits two different regimes: (i) an initial steep increase (decrease) of the $a(c)$ lattice parameter within the first ~0.1 overall Li insertion, followed by (ii) a much gradual increase (decrease) of the $a(c)$ lattice parameter until the end of discharge. Regime (i) is in line with the single-phase reaction within the limited Li solubility, where the insertion of Li only changes the Li composition of the α-TiO$_2$ phase. Upon entering regime (ii), the β-TiO$_2$ phase starts to form after the α-TiO$_2$ phase becomes saturated with Li.

The Li composition of each phase can be interpolated under the assumption of Vegard's law; here, it is based on the interpolation of the c lattice parameter since it has been shown to vary linearly across the stoichiometries of α-TiO$_2$, β-Li$_{0.5}$TiO$_2$, and γ-LiTiO$_2$ (ref. 4) (Fig. S4†). The evolution of the Li composition of each phase during discharge is shown in Fig. 7, where the dashed grey lines indicate the thermodynamic Li solubility
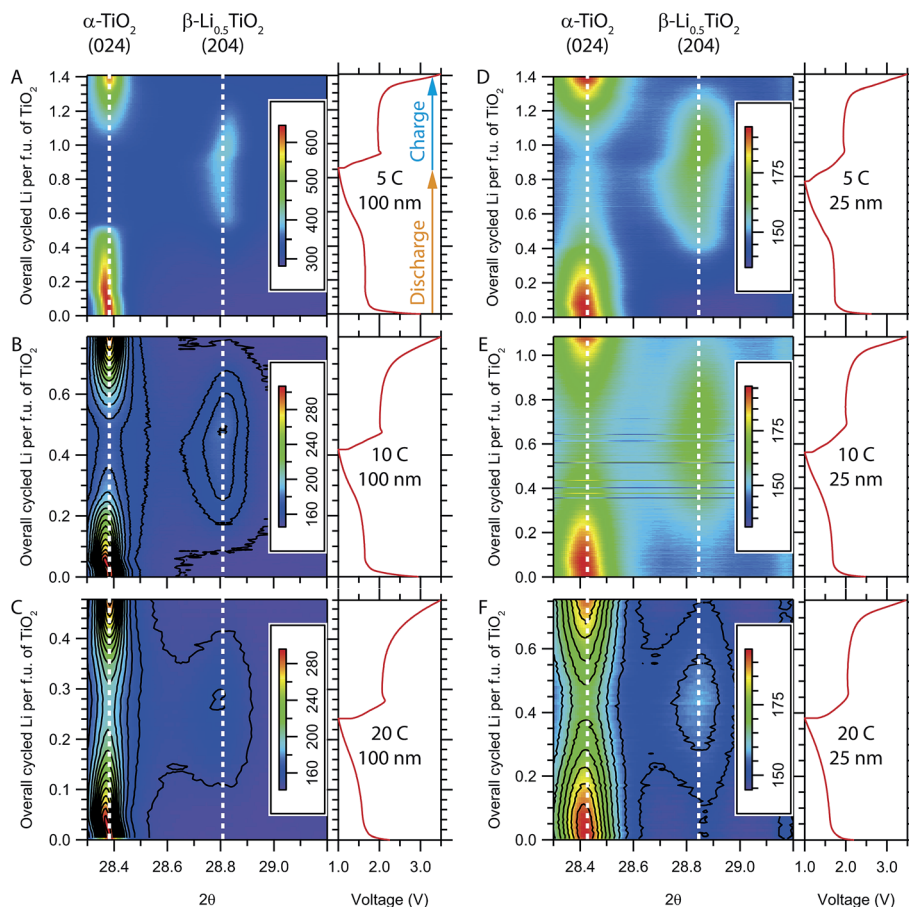
This journal is © The Royal Society of Chemistry 2016

J. Mater. Chem. A, 2016, **4**, 6433–6446 | **6437**

Fig. 5 Image plots showing the time evolution of the *in situ* XRD patterns collected at elevated temperature (~80 °C) for (A–C) 100 nm and (D–F) 25 nm TiO₂ particles at various cycling rates. The intensity scale is shown by the colour bar. The electrochemical profile is shown in the graph to the right of each image. The 2θ region for the (024) reflection of α-TiO₂ and the (204) reflection of β-Li$_{0.5}$TiO₂ is shown. Equally spaced intensity contours (11 levels in total) are drawn in black in B, C and F to aid visual inspection.

limits determined from neutron diffraction studies of 120 nm particles.[4] The Li composition of the saturated α-TiO₂ (see for example in Fig. 7A for the discharge processes of 100 nm at room temperature at the overall Li composition of ~0.07) and that of the emerging β-Li$_{0.5}$TiO₂ phase (at the overall Li composition of ~0.15) exceeds the thermodynamic Li solubility limit. Furthermore, as also shown in Fig. 7A, the Li composition of the saturated α-TiO₂ phase (at the overall Li composition of 0.07–0.1) increases progressively with cycle rate: the maximum Li composition of the α-TiO₂ phase before the formation of the β-TiO₂ phase is found to be $z = 0.042$, 0.045, and 0.054 for 1C, 2C and 5C, respectively, where z is the Li composition of Li$_z$-TiO₂. This rate-dependent solubility is similar to what was observed[2] and predicted[19] for LiFePO₄ at moderately high rates, and is attributed to the overpotential induced by the high current. In comparison, the same, yet less pronounced, rate-induced solubility is observed at higher temperature: for example, for the 100 nm particles cycled at 5C at 80 °C (Fig. 7B), the maximum Li composition of the α-TiO₂ phase before the β-Li$_{0.5}$TiO₂ phase is formed is less than that at room temperature (Li$_{0.035}$TiO₂ is observed at an overall Li composition of ~0.17 at 80 °C, whereas Li$_{0.054}$TiO₂ is seen at an overall Li composition of 0.1 in Fig. 7A). The Li composition of the emerging β-Li$_{0.5}$TiO₂

phase is also closer to the thermodynamic limit than that at room temperature. A similar observation is also made for the 25 nm particles at 80 °C in Fig. 7D. The Li composition of α-TiO₂ increases even after the appearance of β-Li$_{0.5}$TiO₂, especially at the end of the voltage plateau. For example, in Fig. 7A the Li composition of α-TiO₂ during 1C discharge increases substantially after inserting more than 0.2 Li per f.u., which coincides with the end of the voltage plateau. As more α-TiO₂ is transformed to β-Li$_{0.5}$TiO₂, transformation of the residual α-TiO₂ to β-Li$_{0.5}$TiO₂ becomes more difficult and requires a higher overpotential, which then allows more Li to be inserted in α-TiO₂.

The less pronounced rate-induced Li solubility at the higher temperature reflects the kinetic nature of this phenomenon, which is associated with the finite Li diffusivity in the α-TiO₂ and β-Li$_{0.5}$TiO₂ phases: a system not subject to kinetic limitations will always be found in its thermodynamic equilibrium state, and the Li composition of the α-TiO₂ and β-Li$_{0.5}$TiO₂ phases will not exceed their thermodynamic solubilities if the Li diffusion, which has been found to be limited by the Li migration across the α-TiO₂/β-Li$_{0.5}$TiO₂ interface,[20] is infinitely fast. As the diffusion of Li becomes faster with increasing temperature, the Li solubilities of α-TiO₂ and β-Li$_{0.5}$TiO₂ will approach their thermodynamic limits.
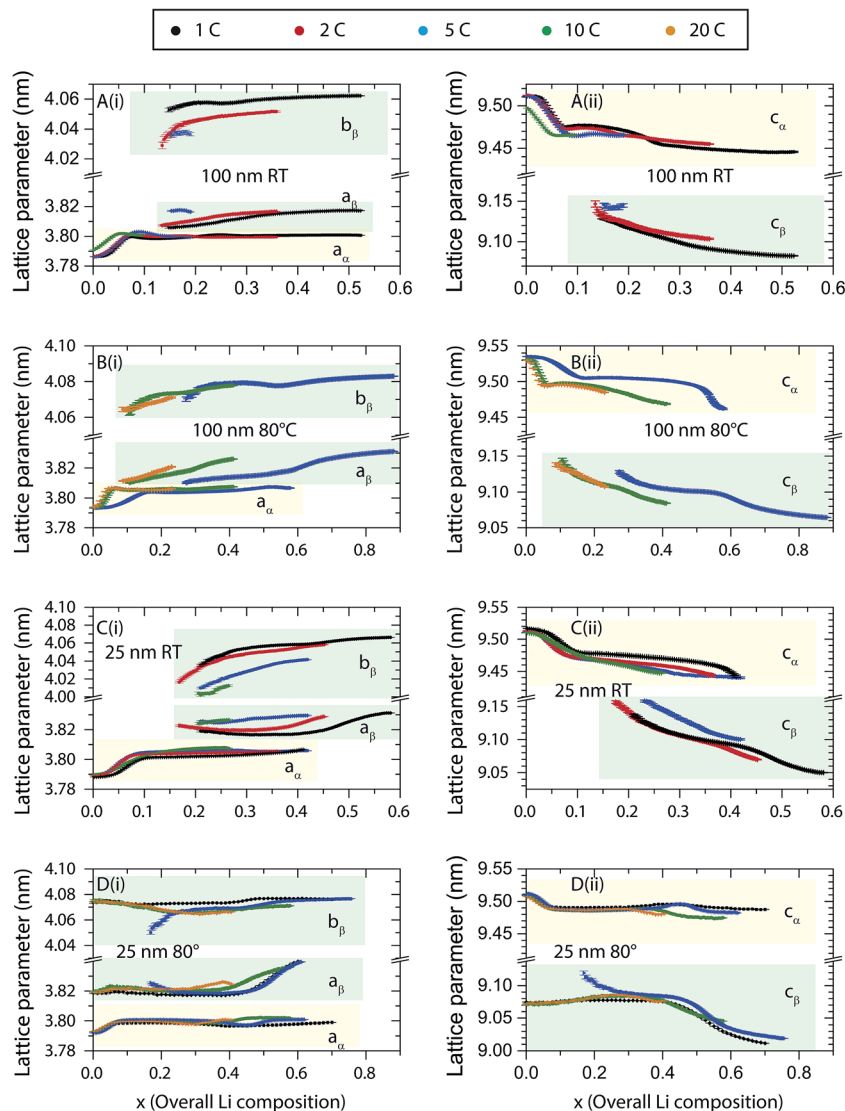
6438 | *J. Mater. Chem. A*, 2016, **4**, 6433–6446

This journal is © The Royal Society of Chemistry 2016

Fig. 6 Lattice parameters of both α-TiO₂ (highlighted in yellow and labelled with the subscript α) and β-Li₀.₅TiO₂ (highlighted in green and labelled with the subscript β) phases obtained from Rietveld refinements for both the room temperature (RT) and the 80 °C discharge processes.

Microstructural evolution of anatase TiO₂ particles during discharge

Although the *in situ* XRD patterns clearly show the presence of only two phases, it is not obvious as to what occurs on the particle level: does the reaction proceed particle by particle or simultaneously in all particles? To answer this question, microstructural analysis was performed based on the FWHM of the (024), (116) and (220) reflections of the α-TiO₂ phase and the (011), (204) and (220) reflections of the β-Li₀.₅TiO₂ phase. These reflections were selected because there is no or only a small amount of overlap with other reflections, in order to minimise ambiguity and correlation in the peak fitting process. The results from fitting individual reflections including the FWHM and the domain size calculated from Scherrer formula, and the phase fractions obtained from Rietveld refinements are presented and discussed below.

100 nm TiO₂ particles

The fitting results for 100 nm particles are shown in Fig. 8 and 9 for the discharge at room temperature and 80 °C, respectively. Typical fitting patterns can be found in Fig. S5.† For 100 nm particles cycled at a rate of 1C at room temperature (Fig. 8A(i)), the (024), (116) and (220) reflections of the α-TiO₂ phase become broader as more Li is inserted. Meanwhile, as shown in Fig. 8A(ii), the (011) reflection of the β-Li₀.₅TiO₂ phase decreases in FWHM, the (204) reflection remaining almost constant in FWHM and the (220) reflection showing an increase in FWHM for insertion of more than 0.25 overall Li composition. Since β-Li₀.₅TiO₂ is the newly formed phase, its domain size will only increase (in the case of the two-phase reaction with phase separation inside individual particles) or remain constant (in the case of the particle by particle reaction) as lithiation proceeds, resulting in the narrowing or the invariance of the
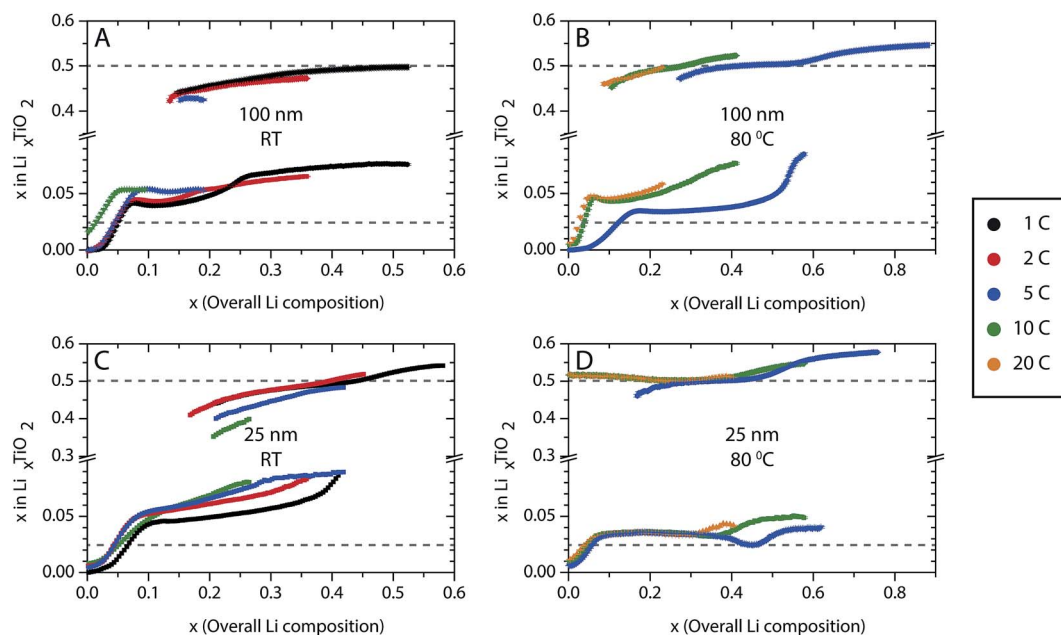
This journal is © The Royal Society of Chemistry 2016

J. Mater. Chem. A, 2016, **4**, 6433–6446 | **6439**

Fig. 7 Evolution of the Li composition in α-TiO$_2$ and β-Li$_{0.5}$TiO$_2$ for (A and B) 100 nm and (C and D) 25 nm particles during discharge. Room temperature (RT) results are shown in A and B, and elevated temperature experiments are shown in B and D. The dashed grey lines indicate the positions for Li solubilities of 0.025 and 0.5, which are considered as the boundaries of the thermodynamic Li solubility.[4] The error bars are smaller than the symbols.
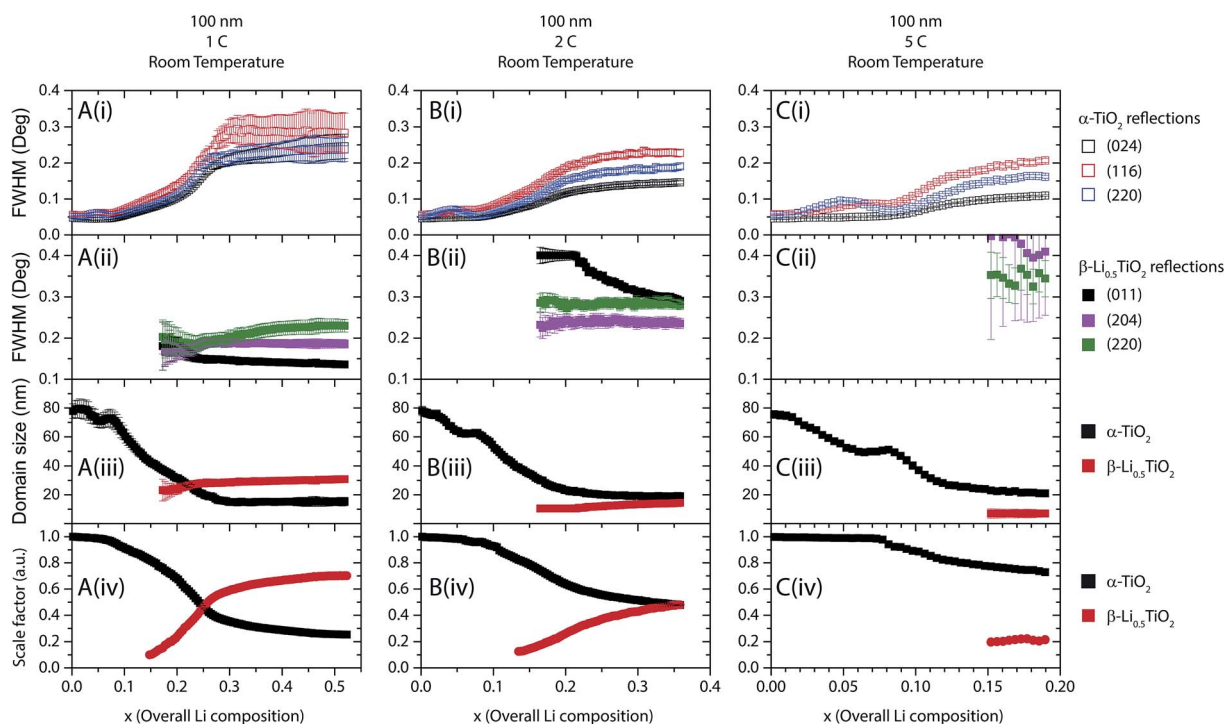

Fig. 8 The evolution of the FWHM of select reflections from both α-TiO$_2$ and β-Li$_{0.5}$TiO$_2$ (i and ii), the domain size determined from the FWHM of the (116) reflection for α-TiO$_2$ and the (011) reflection for β-Li$_{0.5}$TiO$_2$ (iii), and scale factor (iv) as a function of the overall inserted Li for 100 nm particles during discharge at cycle rates of (A) 1C, (B) 2C and (C) 5C at room temperature.

peak width, respectively. The non-monotonic change in the FWHM of the β-Li$_{0.5}$TiO$_2$ (220) reflection suggests that the dominant peak broadening mechanism is microstrain rather than domain size broadening. In fact, the FWHM observed at the beginning of lithiation for all the select α-TiO$_2$ reflections is only 0.05° (2θ), yet the FWHM of the select β-Li$_{0.5}$TiO$_2$ reflections, with the exception of the (011) reflection during 5C discharge at 80 °C (Fig. 9A), are all larger than 0.1° (2θ). Hence,

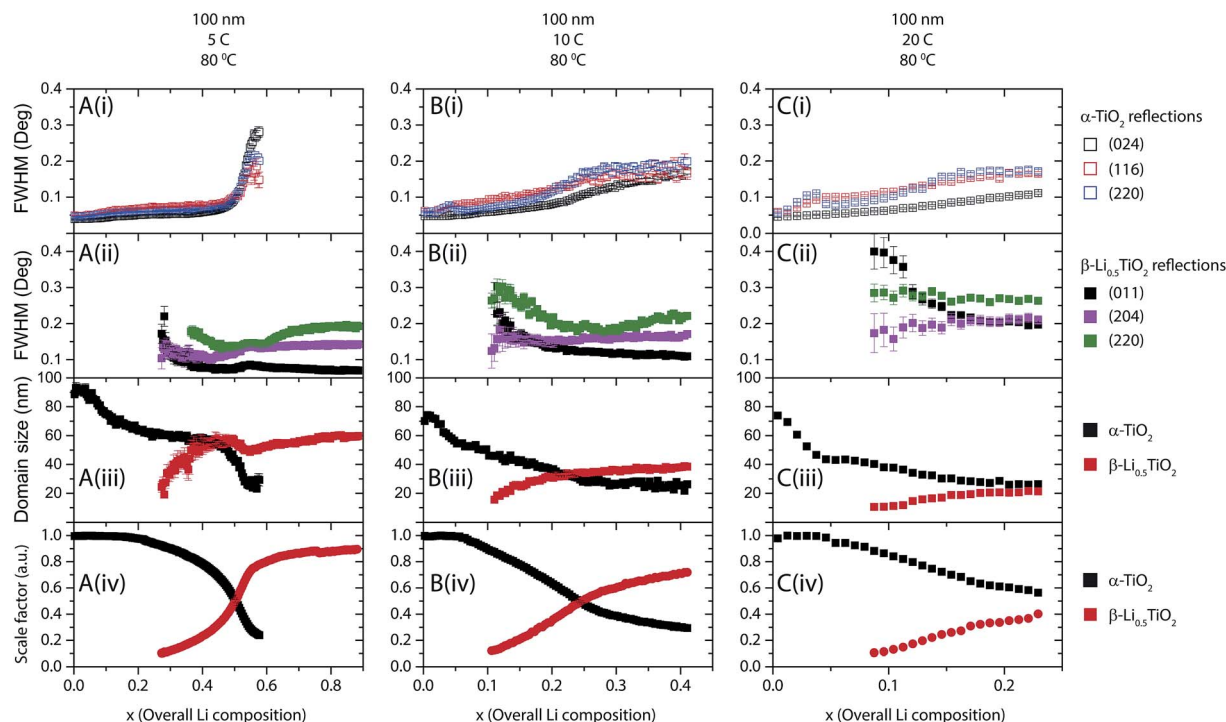6440 | J. Mater. Chem. A, 2016, 4, 6433–6446

This journal is © The Royal Society of Chemistry 2016

Fig. 9 The evolution of the FWHM of select reflections from both α-TiO$_2$ and β-Li$_{0.5}$TiO$_2$ (i and ii), the domain size determined from FWHM of the (116) reflection for α-TiO$_2$ and the (011) reflection for β-Li$_{0.5}$TiO$_2$ (iii), and scale factor (iv) as a function of the overall inserted Li for 100 nm particles during discharge at cycle rates of (A) 5C, (B) 10C and (C) 20C at 80 °C.

the β-Li$_{0.5}$TiO$_2$ reflections are substantially broadened by microstrain. Previous studies find an increase in the length of the zig–zag Ti–O–Ti chain along the b axis when Li is intercalated.[5] This leads to 7% increase and 4% decrease in the b and c lattice parameters, respectively, but only a 0.5% increase in the a lattice parameter when α-TiO$_2$ is transformed to β-Li$_{0.5}$TiO$_2$. Hence, the inter-planar spacings for lattice planes that are not parallel to the b–c plane are susceptible to large variations when the Li composition is not homogeneous, that lack of homogeneity being likely caused by slow Li diffusion in β-Li$_{0.5}$TiO$_2$.[7]

If the broadening of all the select reflections is assumed to be due largely to the finite domain size effect, the domain size of each phase can be deduced using the Scherrer formula. Fig. 8A(iii) shows the evolution of the domain size deduced from FWHM of the (116) reflection of α-TiO$_2$ and the (011) reflection of β-Li$_{0.5}$TiO$_2$. It is seen that the domain size of α-TiO$_2$ decreases from 80 nm to 73 nm from an overall Li composition of 0 to 0.07. This slight initial apparent decrease of 7 nm in the domain size of α-TiO$_2$ is again attributed to the microstrain induced by Li composition variation within the limited solid solution of α-TiO$_2$, because α-TiO$_2$ is the only phase present when the overall Li composition is between 0 and 0.07, i.e. there can be no size-induced broadening. Further Li insertion results in a drastic decrease in the domain size of α-TiO$_2$ from 73 nm to 16 nm towards the end of lithiation, while the domain size of β-Li$_{0.5}$TiO$_2$ grows to 30 nm. The growth of the β-Li$_{0.5}$TiO$_2$ domain at the expense of the α-TiO$_2$ one is expected for a two-phase reaction with the nucleation and growth of a second phase within the particles of the first phase. The fact that this process

is captured by powder XRD, which measures a large number of crystallites at a time, indicates the two-phase reaction occurs simultaneously in all particles. Although the domain size of β-Li$_{0.5}$TiO$_2$ at the end of lithiation appears to be small, even though it constitutes 70% of the total phase fraction (Fig. 8A(iv)), the small domain size (30 nm) of β-Li$_{0.5}$TiO$_2$ could be the result of more than one α-TiO$_2$/β-Li$_{0.5}$TiO$_2$ interface per particle[20] and/or a concurrent microstrain broadening due to the Li composition variation of β-Li$_{0.5}$TiO$_2$.

As shown in Fig. 8B and C, increasing the cycling rate to 2C and 5C does not qualitatively change the behaviour of FWHM of the reflections: the α-TiO$_2$ reflections increase while the β-Li$_{0.5}$TiO$_2$ reflections decrease or remain constant in FWHM with increasing overall Li composition, indicating the same two-phase reaction with the 1C discharge. It is noted that FWHM of the β-Li$_{0.5}$TiO$_2$ reflections increases with the cycling rate: for example, as shown in Fig. 8A–C(ii), the FWHM of the (204) reflection of β-Li$_{0.5}$TiO$_2$ is 0.19°, 0.36°, and 0.4° (2θ) for 1C, 2C, and 5C, respectively, suggesting the formation of smaller β-Li$_{0.5}$TiO$_2$ domains or larger microstrain with increasing rate. Broad reflections with weak intensities can lead to large uncertainties in the determination of FWHM, as can be seen in the fitting pattern for the β-Li$_{0.5}$TiO$_2$ (011) reflection (whose FWHM is not presented in Fig. 8C for this reason) in Fig. S5C† for the overall Li composition of 0.19 during 5C discharge at room temperature. As with discharge at room temperature, cycles at 80 °C for 100 nm particles (Fig. 9) still proceed by a two-phase reaction, the α-TiO$_2$ domain size decreasing and the β-Li$_{0.5}$TiO$_2$ domain size increasing with increasing overall Li

This journal is © The Royal Society of Chemistry 2016

J. Mater. Chem. A, 2016, 4, 6433–6446 | 6441

composition. Our observation is consistent with the previous room temperature *in situ* XRD study,[9] which reported a two-phase mechanism for the phase transition of 130 nm anatase TiO_2 particles at a discharge rate of C/120. The simultaneous nucleation in all particles, as opposed to particle by particle nucleation, is attributed to the much higher rate applied in this study.

The lithiation process of 100 nm TiO_2 particles is summarised in Fig. 10: (i) lithiation starts with a single phase reaction in the α-TiO_2 phase, followed by (ii) simultaneous nucleation of β-$Li_{0.5}TiO_2$ domains in all particles; (iii) the β-$Li_{0.5}TiO_2$ domains continue to grow until all the α-TiO_2 domains are transformed into β-$Li_{0.5}TiO_2$.

25 nm TiO_2 particles

The fitting results for 25 nm particles are shown in Fig. 11 and 12 for cycles at room temperature and 80 °C, respectively. Typical peak fitting results can be found in Fig. S6.† During room temperature 1C discharge (Fig. 11A(i)) the FWHM of the α-TiO_2 reflections increases from 0.2° to 0.3° (2θ) from an overall Li composition of 0 to 0.4. The evolution of the β-$Li_{0.5}TiO_2$ reflections, shown in Fig. 11A(ii), follows the same trend as observed for the 100 nm particles: the FWHM of the (011) and (204) reflections decreases with increasing overall Li composition, while the FWHM of the (220) reflection decreases first until the overall Li composition reaches 0.45, after which it increases again. Fig. 11A(iii) shows the domain size as a function of overall Li composition deduced from the FWHM of the (116) reflection of α-TiO_2 and the (011) reflection of β-$Li_{0.5}TiO_2$. As shown in Fig. 11A(iii) for a 1C discharge, the domain size of α-TiO_2 decreases from 23 to 15 nm when the overall Li composition increases from 0 to 0.4, meanwhile the phase fraction of α-TiO_2 decreases by 80%. If the two phases in a spherical particle assume a core–shell morphology, where the core is α-TiO_2 and the shell is β-$Li_{0.5}TiO_2$, the volume fraction of a 15 nm diameter spherical core of α-TiO_2 in a 23 nm diameter spherical particle would correspond to 28%, which is very close to the 20% phase fraction of the α-TiO_2 phase. However, this core–shell

arrangement would leave a shell (β-$Li_{0.5}TiO_2$) of 4 nm thick, which is far less than the value, 17 nm, determined from the Scherrer formula. Therefore, the only plausible explanation is that the lithiation takes place particle by particle and the decrease in the domain size of α-TiO_2 from 23 nm to 15 nm is associated with the microstrain developed in α-TiO_2. This microstrain could result from the distortion present in the α-TiO_2 phase and/or the Li composition variation between different α-TiO_2 particles. The particle-by-particle mechanism also stipulates a constant domain size for β-$Li_{0.5}TiO_2$, hence, the very large broadening at the point where the β-$Li_{0.5}TiO_2$ peaks emerge is also associated with the microstrain effect, which is likely to be caused by compositional variation between β-$Li_{0.5}TiO_2$ particles. Reactions at higher rates, shown in Fig. 11B for 2C and Fig. 11C for 5C, exhibit qualitatively similar behaviour and also proceed particle by particle. The domain size of β-$Li_{0.5}TiO_2$ at 5C discharge (Fig. 11C) is 12 nm at the overall Li composition of 0.4, well below 20 nm observed at the end charge for cycle rates of 1C and 2C, despite the dominant presence of the β-$Li_{0.5}TiO_2$ phase. Hence, this provides a direct evidence for the presence of microstrain in β-$Li_{0.5}TiO_2$.

When the temperature is raised to 80 °C, for example, for the cycle rate of 5C as shown in Fig. 12A(i), the FWHM of the (024) reflection of α-TiO_2 remains almost constant at ~0.18° throughout the entire overall Li composition, while the FWHM of the (116) and (220) reflections of α-TiO_2, after a rapid initial increase from 0 to 0.07 overall Li, which is attributed to the microstrain effect, also shows very little change over the rest of the overall Li composition range. As shown in Fig. 12A(ii), the FWHM of the (011) reflection of β-$Li_{0.5}TiO_2$ decreases monotonically with increasing overall Li composition, whereas the FWHM of the (204) and (220) reflections decreases from 0.2 to 0.45 overall Li composition and increases from 0.45 overall Li composition onwards. The increase in the FWHM of the (204) and (220) reflections of β-$Li_{0.5}TiO_2$ is attributed to the microstrain effect. As shown in Fig. 12A(iii), the domain size of α-TiO_2 determined from FWHM of the (116) reflection of α-TiO_2 remains effectively invariant at ~20 nm except the small initial drop from 23 nm to 20 nm from 0 to 0.07 overall Li composition.
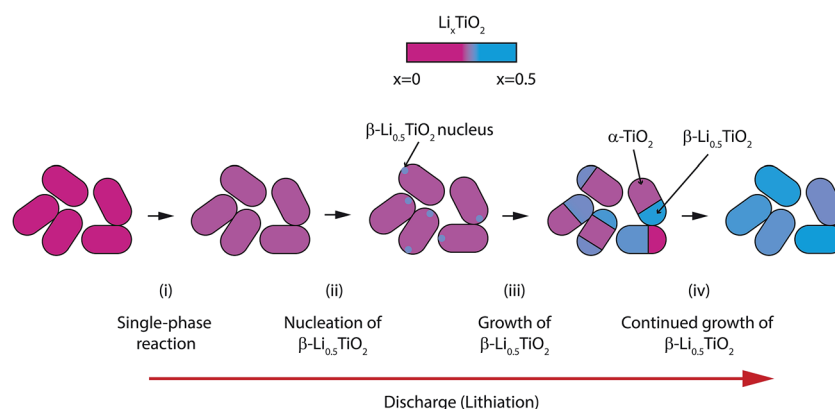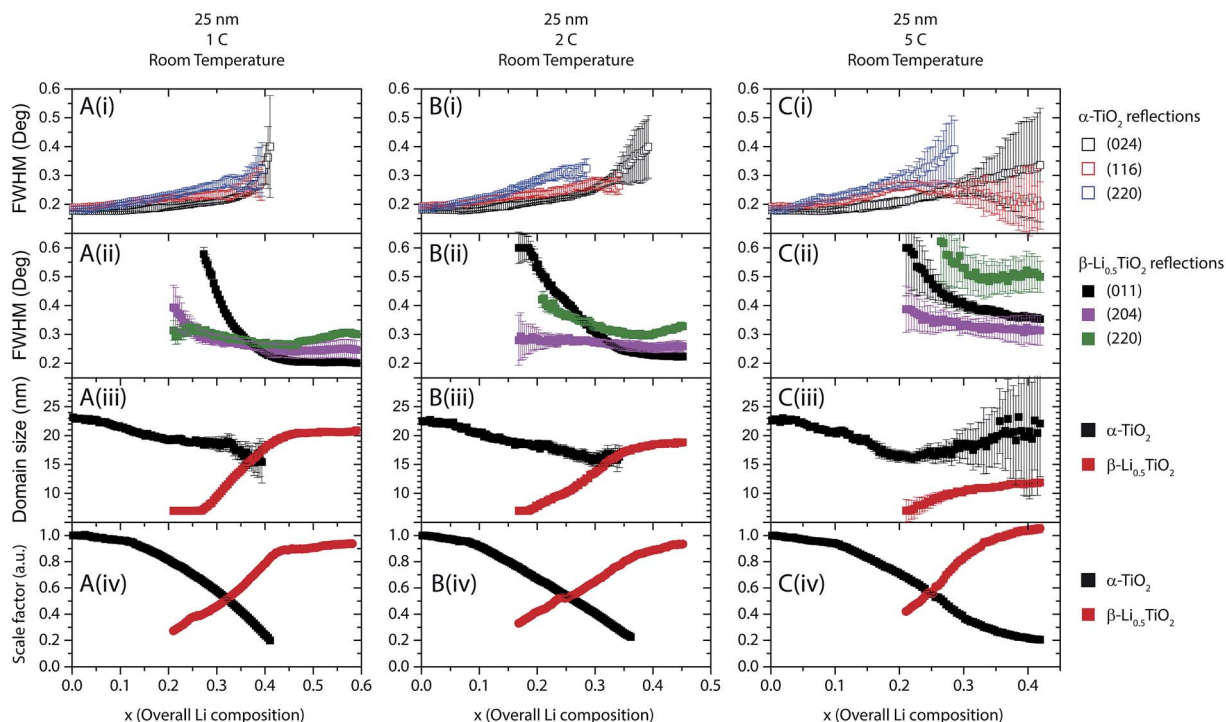

Fig. 10 Schematic illustration of the phase transition occurring in 100 nm anatase TiO_2 particles during high rate discharge. The lithiation proceeds firstly by a solid solution reaction in the α-TiO_2 phase (i) followed by the nucleation of β-$Li_{0.5}TiO_2$ (ii). The β-$Li_{0.5}TiO_2$ domains grow in size until the entire particle comprises a single phase (iii and iv).

Fig. 11 The evolution of the FWHM of select reflections from both α-TiO$_2$ and β-Li$_{0.5}$TiO$_2$ (i and ii), the domain size determined from the FWHM of the (116) reflection for α-TiO$_2$ and the (011) reflection for β-Li$_{0.5}$TiO$_2$ (iii), and scale factor (iv) as a function of the overall inserted Li for 25 nm particles during discharge at cycle rates of (A) 1C, (B) 2C and (C) 5C discharge at room temperature.
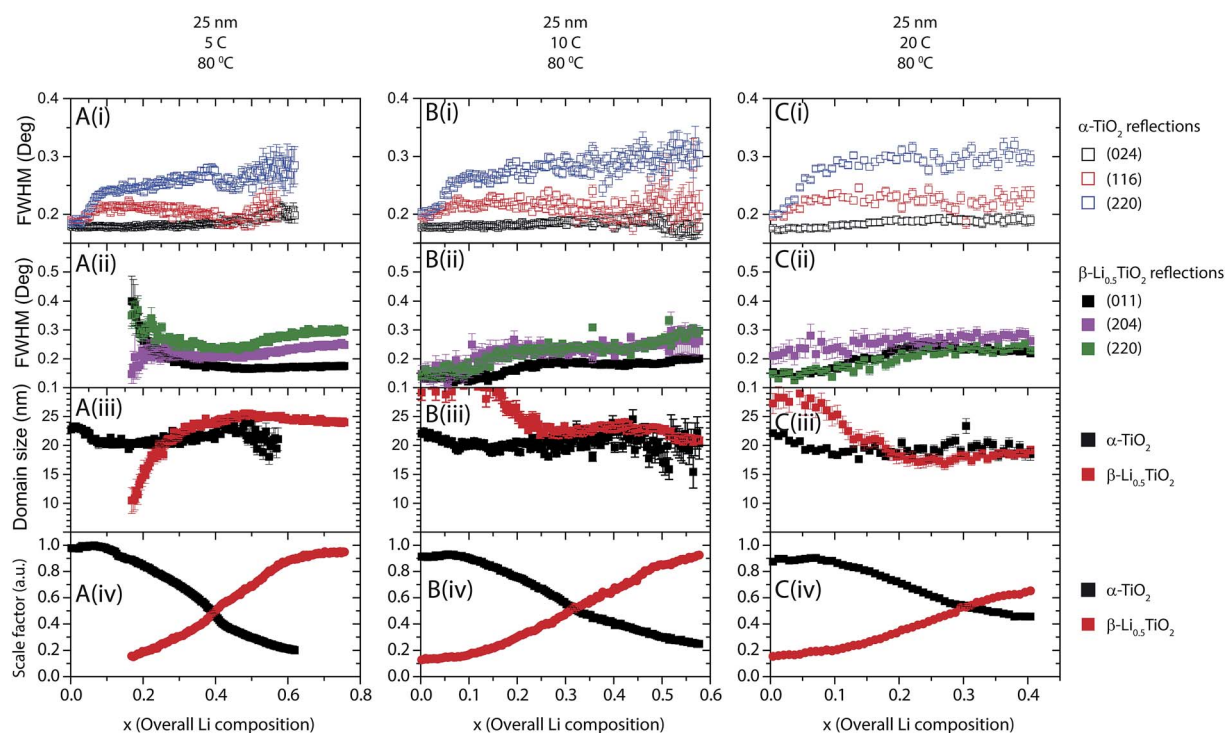
Fig. 12 The evolution of the FWHM of select reflections from both α-TiO$_2$ and β-Li$_{0.5}$TiO$_2$ (i and ii), the domain size determined from the FWHM of the (116) reflection for α-TiO$_2$ and the (011) reflection for β-Li$_{0.5}$TiO$_2$ (iii), and scale factor (iv) as a function of the overall inserted Li for 25 nm particles during discharge at cycle rates of (A) 5C, (B) 10C and (C) 20C discharge at 80 °C.

Since the 10C and 20C discharge was carried out consecutively on the same cell after the cycle at 5C, a small amount ($\sim$10%) of the β-$Li_{0.5}TiO_2$ phase (residual β-$Li_{0.5}TiO_2$), which did not transform back to α-TiO_2, was present at the beginning of 10C and also 20C discharge (shown in Fig. S6C† for 10C charge). The presence of the residual β-$Li_{0.5}TiO_2$ phase complicates the interpretation of the FWHM of the β-$Li_{0.5}TiO_2$ reflections: the increase, as opposed to the decrease as observed at all other rates, in the FWHM of the β-$Li_{0.5}TiO_2$ reflections, as shown in Fig. 12B(ii) and C(ii) for 10C and 20C, respectively, is attributed to the formation of β-$Li_{0.5}TiO_2$ particles that are not compositionally homogeneous. Nonetheless, interpretation of the FWHM of the α-TiO_2 reflections and the deduced domain size of α-TiO_2, is not affected: the effectively invariant domain size ($\sim$20 nm) of α-TiO_2 throughout the entire overall Li composition for the 10C and 20C discharge, shown in Fig. 12B(iii) and C(iii), respectively, is consistent with the particle-by-particle reaction mechanism.

The particle-by-particle reaction mechanism is in agreement with the previous findings from *in situ*[9] and *ex situ*[4] XRD studies of anatase TiO_2 nanoparticles (15 nm and <40 nm, respectively), and is attributed to the relatively high energy of the α-TiO_2/β-$Li_{0.5}TiO_2$ interface, whose disappearance reduces the total energy of the system. Fig. 13 summarises the lithiation process: (i) the initial lithiation involves a single phase reaction in the α-TiO_2 phase; (ii) further lithiation triggers the transformation of an entire α-TiO_2 domain into a β-$Li_{0.5}TiO_2$ one (stages (ii–iv)). This transformation does not occur simultaneously in all particles but proceeds from particle to particle until every particle is transformed.

Discussion on the nature of the "instantaneous" α-TiO_2 to β-$Li_{0.5}TiO_2$ phase transition of 25 nm TiO_2 particles

What remains unanswered from the preceding sections is the microscopic process by which an entire α-TiO_2 domain transforms into a β-$Li_{0.5}TiO_2$ one. Analogous to the case for $LiFePO_4$ nanoparticles, two mechanisms need to be examined: (i) phase

transition by a continuous structural change from α-TiO_2 to β-$Li_{0.5}TiO_2$, and (ii) nucleation of β-$Li_{0.5}TiO_2$ in α-TiO_2 domain followed immediately (*i.e.*, essentially instantaneous) by the fast propagation of the phase boundary (the domino-cascade mechanism[10]).

Since the transformation from α-TiO_2 to β-$Li_{0.5}TiO_2$ involves a change in crystal symmetry from $I4_1/amd$ to $Imma$, corresponding to a group–subgroup relationship, a continuous path, if there is one, between the two phases must undergo a second-order phase transition. Although a continuous structural transition between α-TiO_2 and β-$Li_{0.5}TiO_2$ is found, with the use of the programme ISOTROPY,[21] to be allowed by Landau theory,[22] whether it will occur depends on the energetics and kinetics of various transition pathways.

The Gibbs free energy diagram for different phase transition paths is displayed in Fig. 14. If the transformation from α-TiO_2 to β-$Li_{0.5}TiO_2$ proceeds by a continuous overpotential driven structural phase transition, the energy will evolve along the solid black curve during lithiation: the initial lithiation involves the single-phase reaction of α-TiO_2 until it reaches the critical point O, beyond which the energy for the high symmetry phase (α-TiO_2) becomes higher than the low symmetry one (β-$Li_{0.5}TiO_2$). Therefore, traversing across point O from left to right along the solid black line, the entire nanoparticle will first transform to a lower symmetry (orthorhombic) phase, and then continue to be lithiated *via* a single-phase reaction. This transition across point O should manifest itself in the XRD measurement as the branching of a single ($0kl$) (l can be 0) reflection into two separate, ($0kl$) and ($h0l$), reflections, which is characteristic of a continuous structural (second-order) transition. In the case studied here, no branching of the (024) reflection of α-TiO_2 into the (024) and (204) reflections of β-$Li_{0.5}TiO_2$ is observed. In addition, cycling at 10C and 20C should have induced an appreciable fraction of the TiO_2 particles to react at a time, as observed for $LiFePO_4$,[1,2] if a continuous structural transition did take place.

If the transformation takes place *via* a nucleation and growth mechanism, which is found to be the case in this work, the Li
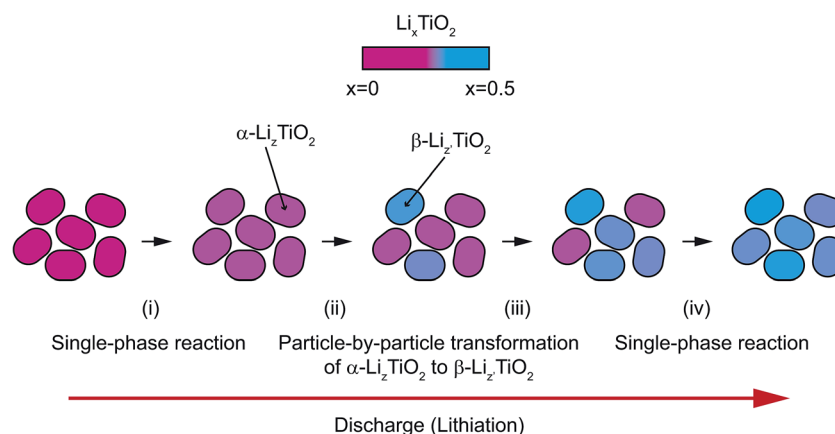

Fig. 13 Schematic illustration of the phase transition occurring in 25 nm anatase TiO_2 particles during high rate discharge. Lithiation proceeds firstly by a solid solution reaction in the α-TiO_2 phase (i) followed by the sequential (particle-by-particle) transformation from α-Li_zTiO_2 to β-$Li_{z'}TiO_2$ particles (ii–iv), where $z > 0.025$ and $z' < 0.5$.

6444 | *J. Mater. Chem. A*, 2016, 4, 6433–6446
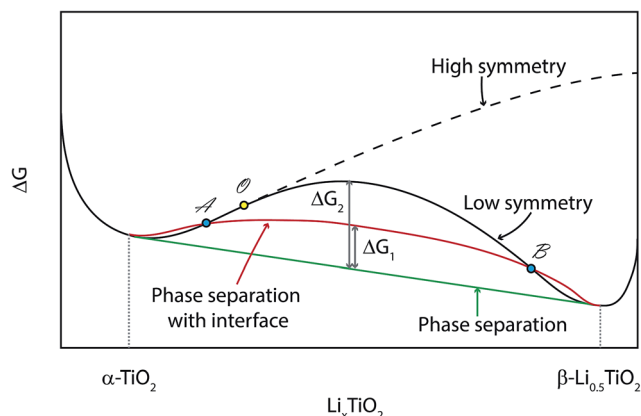
This journal is © The Royal Society of Chemistry 2016

Fig. 14 Illustration of the change in Gibbs free energy for various phase transition paths. The solid black line represents a continuous structural transition (second-order phase transition), and the critical point is marked by ○ (solid yellow circle). The dashed black line is the projected energy curve if there is no reduction to lower symmetry. The solid green line is the common tangent construction that determines the lowest possible energy of a system with a mixture of α-TiO$_2$ and β-Li$_{0.5}$TiO$_2$ not coexisting in the same particle. The solid red line is the modified energy of a system with a mixture of α-TiO$_2$ and β-Li$_{0.5}$TiO$_2$ separated by a phase boundary.

composition in the nanoparticle will evolve along the solid red curve, which differs from the equilibrium energy (solid green) only by an α-TiO$_2$/β-Li$_{0.5}$TiO$_2$ interfacial energy, ΔG_1. Phase separation will be induced within the composition between A and B, *i.e.* between the points where the red curve crosses the black curve. Consequently, the lithiation process is limited by the rate of nucleation.

Kinetics aside, the transformation should take the route that lies lower in energy, and it is possible that the energy barrier for the second-order phase transition (solid black curve) is too high for it to occur. In addition, the interfacial energy, ΔG_1, can be minimised by forming an interface along a zero-strain plane,[7] hence favouring the two-phase mechanism with a fast propagation of the interface. In this work, when Li diffusion is improved at high temperature, the lithiation process becomes almost independent of the cycling rate and remains distinctively two-phase, *i.e.* the lattice parameters of each phase remain almost invariant in the regime when both phases are present, as seen in Fig. 6D. This observation suggests any lattice parameter deviation from equilibrium values observed for the room temperature cycling is primarily due to slow Li diffusion, which is found to cause deviations in lattice parameters even during lithiation at a rate of C/120.[9] It must be pointed out that the deviation from equilibrium observed here is fundamentally different from the non-equilibrium phase transition observed for LiFePO$_4$ at high rates: the non-equilibrium phase transition of LiFePO$_4$ is rooted in the small energy difference between the equilibrium and non-equilibrium phase transition path,[23] which is not available to anatase TiO$_2$.

Conclusions

The lithiation mechanism of anatase TiO$_2$ particles during Li insertion was investigated by *in situ* XRD as a function of rate,

particle size and cycling temperature. Li solubilities of the end member phases, α-TiO$_2$ and β-Li$_{0.5}$TiO$_2$, are found to increase noticeably with increasing rate, yet no continuous transition from α-TiO$_2$ to β-Li$_{0.5}$TiO$_2$ is observed, even at a cycle rate of 20C, in contrast to the behaviour observed for LiFePO$_4$.[1,2] An increase in temperature from room temperature to 80 °C results a significant improvement in the electrode's electrochemical performance although the reaction still proceeds by a two-phase reaction. The Li solubility exceeds the thermodynamic limit and increases with cycling rate for both the α-TiO$_2$ and β-Li$_{0.5}$TiO$_2$ phases, due to the kinetic limitation imposed by the finite Li diffusivity. Domain size information obtained from the line broadening analysis reveals a change in the phase transition mechanism brought about by a reduction in particle size from 100 nm to 25 nm: the 100 nm particles react simultaneously *via* a conventional nucleation and growth (two-phase) mechanism, while the 25 nm particles react sequentially again *via* a two-phase, domino-cascade mechanism. (De)lithiation *via* a first-order rather than a second-order phase transition may be inherent in phase-separating compounds with end member phases of different symmetries. The lack of a continuous structural phase transition may hinder the reaction kinetics, and the search for high-rate electrode materials should be focused on compounds exhibiting no phase separation or phase-separating compounds with isostructural end member phases.

Notes and references

1 H. Liu, F. C. Strobridge, O. J. Borkiewicz, K. M. Wiaderek, K. W. Chapman, P. J. Chupas and C. P. Grey, *Science*, 2014, **344**, 1252817.
2 X. Zhang, M. van Hulzen, D. P. Singh, A. Brownrigg, J. P. Wright, N. H. van Dijk and M. Wagemaker, *Nano Lett.*, 2014, **14**, 2279–2285.
3 A. Singer, A. Ulvestad, H. Cho, J. W. Kim, J. Maser, R. Harder, Y. S. Meng and O. G. Shpyrko, *Nano Lett.*, 2014, **14**, 5295–5300.

This journal is © The Royal Society of Chemistry 2016

J. Mater. Chem. A, 2016, **4**, 6433–6446 | **6445**

4 M. Wagemaker, W. J. H. Borghols and F. M. Mulder, *J. Am. Chem. Soc.*, 2007, **129**, 4323–4327.

5 M. Wagemaker, G. J. Kearley, A. A. Van Well, H. Mutka and F. M. Mulder, *J. Am. Chem. Soc.*, 2003, **125**, 840–848.

6 D. Murphy, R. Cava, S. Zahurak and A. Santoro, *Solid State Ionics*, 1983, **9–10**, 413–417.

7 A. A. Belak, Y. Wang and A. Van Der Ven, *Chem. Mater.*, 2012, **24**, 2894–2898.

8 W. J. H. Borghols, D. Lützenkirchen-Hecht, U. Haake, E. R. H. van Eck, F. M. Mulder and M. Wagemaker, *Phys. Chem. Chem. Phys.*, 2009, **11**, 5742–5748.

9 K. Shen, H. Chen, F. Klaver, F. M. Mulder and M. Wagemaker, *Chem. Mater.*, 2014, **26**, 1608–1615.

10 C. Delmas, M. Maccario, L. Croguennec, F. Le Cras and F. Weill, *Nat. Mater.*, 2008, **7**, 665–671.

11 O. J. Borkiewicz, B. Shyam, K. M. Wiaderek, C. Kurtz, P. J. Chupas and K. W. Chapman, *J. Appl. Crystallogr.*, 2012, **45**, 1261–1269.

12 A. A. Coelho, *TOPAS v2.0: General profile and structure analysis software for powder diffraction data*, Karlsruhe, 2000.

13 M. Järvinen, *J. Appl. Crystallogr.*, 1993, **26**, 525–531.

14 T. Ohzuku, T. Kodama and T. Hirai, *J. Power Sources*, 1985, **14**, 153–166.

15 Y.-G. Guo, Y.-S. Hu and J. Maier, *Chem. Commun.*, 2006, 2783–2785.

16 J. S. Chen, Y. L. Tan, C. M. Li, Y. L. Cheah, D. Luan, S. Madhavi, F. Y. C. Boey, L. A. Archer and X. W. Lou, *J. Am. Chem. Soc.*, 2010, **132**, 6124–6130.

17 X. P. Gao, Y. Lan, H. Y. Zhu, J. W. Liu, Y. P. Ge, F. Wu and D. Y. Song, *Electrochem. Solid-State Lett.*, 2005, **8**, A26.

18 G. Sudant, E. Baudrin, D. Larcher and J.-M. Tarascon, *J. Mater. Chem.*, 2005, **15**, 1263–1269.

19 P. Bai, D. A. Cogswell and M. Z. Bazant, *Nano Lett.*, 2011, **11**, 4890–4896.

20 M. Wagemaker, R. van de Krol, A. P. Kentgens, A. A. van Well and F. M. Mulder, *J. Am. Chem. Soc.*, 2001, **123**, 11454–11461.

21 H. T. Stokes, D. M. Hatch and B. J. Campbell, *ISOTROPY Software Suite*, iso.byu.edu.

22 L. D. Landau and E. M. Lifshitz, *Statistical Physics*, Pergamon Press, Oxford, 3rd edn, 1980.

23 R. Malik, F. Zhou and G. Ceder, *Nat. Mater.*, 2011, **10**, 587–590.